ACS APPLIED MATERIALS & INTERFACES

Research Article

www.acsami.org

A Noncovalent Compatibilization Approach to Improve the Filler Dispersion and Properties of Polyethylene/Graphene Composites

Alexandros A. Vasileiou, Marianna Kontopoulou,* and Aristides Docoslis

Department of Chemical Engineering, Queen's University, Kingston, Ontario K7L 3N6, Canada

ABSTRACT: Graphene was prepared by low temperature vacuum-assisted thermal exfoliation of graphite oxide. The resulting thermally reduced graphene oxide (TRGO) had a specific surface area of 586 m^2/g and consisted of a mixture of single-layered and multilayered graphene. The TRGO was added to maleated linear low-density polyethylene LLDPE and to its derivatives with pyridine aromatic groups by melt compounding. The LLDPE/TRGO composites exhibited very low electrical percolation thresholds, between 0.5 and 0.9 vol %, depending on the matrix viscosity and the type of functional groups. The dispersion of the TRGO in the compatibilized composites was improved significantly, due to enhanced noncovalent interactions between the aromatic moieties grafted onto the polymer matrix and the filler. Better dispersion resulted in a slight increase in the rheological and electrical percolation thresholds, and to significant improvements in mechanical properties and thermal conductivity, compared to the noncompatibilized composites. The presence of high surface area nanoplatelets within the polymer also resulted in a substantially improved thermal stability. Compared to their counterparts containing multiwalled carbon nanotubes, LLDPE/TRGO composites had lower percolation thresholds. Therefore, lower amounts of TRGO were sufficient to impart electrical conductivity and modulus improvements, without compromising the ductility of the composites.

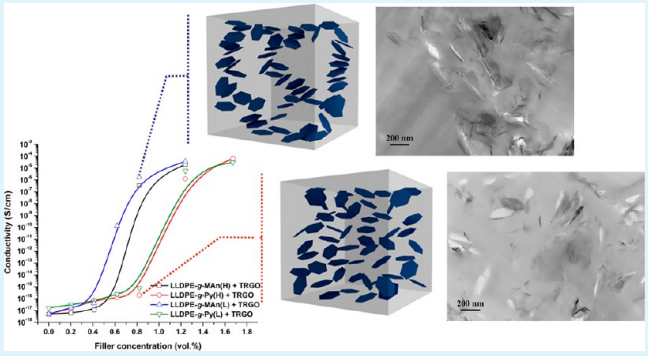

KEYWORDS: *graphene, polyethylene, nanocomposites, viscosity, functionalization, conductivity*

1. INTRODUCTION

Polymer nanocomposites containing conducting carbon structures have attracted great research interest owing to the potential for development of electrically and thermally conductive compounds, suitable for a wide range of value-added applications.[1,2] Graphene in particular possesses unique properties, such as high surface area and aspect ratio, high modulus and exceptional thermal and electrical properties.[3−5] Additionally it is nontoxic under normal conditions, contrary to other sp^2 carbon structures such as nanotubes.[6] These attributes make it a promising additive in polymer composites aiming at the production of novel materials suitable for electronic devices, energy storage, sensors, EMI shielding, and biomedical applications.[7−10]

Bottom-up and top-down processes can be employed to produce graphene.[7,8] Top-down processes commonly involve the production of graphene oxide nanosheets from exfoliation and reduction of graphite oxide (GO) through thermal or chemical means.[9,11,12] They are preferred in polymer composite technology because of their suitability for large scale production.

Addition of graphene to thermoplastics, such as polycarbonate, polyamide, polystyrene, polyimide, PMMA, and so forth,[7,9,12−17] generally results in increases in electrical and thermal conductivity, modulus, as well as improved gas barrier properties. However, these properties are highly dependent upon the degree of dispersion, and generally the reported values are not commensurate with a filler of such a high aspect ratio.[7,9]

In spite of the recent activity, reports on polyolefin/graphene nanocomposites are relatively scarce;[18−24] even more so for the case of melt compounded GO/polyolefins. The latter include polypropylene (PP),[25] high-density polyethylene (HDPE)[26,27] and linear low-density polyethylene (LLDPE).[19] This is due in part to the fact that dispersion of graphene within nonpolar polymers by melt compounding presents a significant challenge, given that these particles are thermodynamically driven to aggregate.[19] Various compatibilization strategies have been employed to achieve improved interfacial adhesion between the filler and the polymer.[25] These include GO[9,22,23,25,28] and polymer matrix functionalization techniques.[19]

Generally covalent functionalization of conductive fillers, such as CNT or graphene tends to disrupt the sp^2-hybridized network required for good electron/hole conduction, thus compromising the electrical conductivity. Noncovalent compatibilization strategies involving weak CH−π and/or $\pi-\pi$ interactions are the preferred choice for tuning the interfacial properties without compromising conductivity.[29−31] Recently, we showed that a noncovalent compatibilization approach, involving the intro-

Received: November 6, 2013
Accepted: January 14, 2014
Published: January 14, 2014

duction of aromatic moieties onto the polymer's backbone, resulted in improved dispersion and mechanical properties in LLDPE/MWCNT composites.[32] The aromatic moieties were able to interact with the MWCNTs by $\pi-\pi$ stacking, thus improving interfacial adhesion between the polyolefin matrix and the MWCNTs.

In this study, thermally reduced graphene oxide (TRGO) was prepared by a low temperature vacuum-assisted thermal exfoliation process[33−35] and incorporated into maleated LLDPE and its amino-pyridine derivatives by melt compounding. The effects of compatibilization and matrix viscosity on the mechanical, thermal, electrical, and rheological properties of the melt compounded LLDPE/TRGO composites are reported. The study concludes with a direct comparison between composites containing TRGO and MWCNT.

2. EXPERIMENTAL SECTION

2.1. Materials. Natural graphite powder (<150 μm, purity 99.99%) was purchased from Aldrich and used as received. Fusabond E439 and E528, which are both maleic anhydride grafted LLDPEs (LLDPE-*g*-MAn) containing 0.5−1.0 wt % grafts and having MFI 2.7 g/10 min and 6.7 g/10 min (190 °C/2.16 kg), respectively, were supplied from E.I. DuPont Canada. These are denoted as LLDPE-*g*-MAn(H) and LLDPE-*g*-MAn(L), representing, respectively, high and low viscosity. 4-Aminomethylpyridine (AMP, 98% purity) was supplied from Aldrich. Nitric acid (70 v/v%), sulfuric acid (98 v/v%), and potassium chlorate (≥99.0%) were supplied from Sigma-Aldrich and were of ACS reagent grade. All materials and solvents were of analytical grade and were used without further purification.

2.2. Synthesis and Characterization of TRGO. Graphite (G) was oxidized using potassium chlorate in a concentrated mixture of nitric/sulfuric acid.[34] Graphite powder (10 g) was added to a homogeneous mixture of concentrated nitric acid (70 mL) and sulfuric acid (130 mL) under vigorous stirring. After uniform dispersion of the graphite powder, 80 g of potassium chlorate was added slowly to avoid the risk of explosion. The reaction was allowed to proceed for 5 days at room temperature. The resulting graphite oxide (GO) was extracted from the solution by filtration, thoroughly washed with deionized water until neutral to litmus and dried at 100 °C in a vacuum oven.

Exfoliation and reduction of the GO was achieved by thermally induced expansion under high vacuum.[33−35] The as-prepared GO was placed in a quartz tube, which was sealed at one end and stoppered at the other end, through which the reaction vessel was connected to a high vacuum pump. Heating of the tube ensued at a fast rate (>50 °C/min) to 300 °C under high vacuum (<0.5 Pa). At this temperature, a very abrupt volume change, indicative of exfoliation, was observed. The sample was kept at 300 °C, and the high vacuum was maintained for 5 h to remove the superabundant oxygen functional groups during the heat treatment by thermal reduction. It has been shown that residual oxygen groups have a very detrimental effect on the electrical properties of graphene.[3,8,36,37]

2.3. Synthesis of LLDPE-*graft*-Aminomethylpyridine (LLDPE-*g*-Py). LLDPE-graft-aminomethylpyridine (LLDPE-*g*-Py) was synthesized in a Haake Rheomix E3000 instrument by reacting LLDPE-*g*-MAn with a molar excess (compared to maleic anhydride grafts) of 4-aminomethylpyridine at 190 °C for 10 min.[32] The resulting polymer was solubilized in xylene at 120 °C and precipitated in methanol to remove the excess of amine bearing molecules. The grafting reaction was confirmed by FTIR spectra obtained using a Vertex 70 FTIR spectrometer (Bruker Optics). Samples were thin films, prepared in a Carver hydraulic hot press at 190 °C and 50 MPa. The detailed characterization of the resulting product is shown elsewhere.[32]

2.4. Melt Compounding. LLDPE nanocomposites containing TRGO were prepared using a DSM Research 5 mL Micro-Compounder (DSM Resolve, Geleen Netherlands), at a temperature of 190 °C, screw speed of 60 rpm, and a mixing time of 10 min. Appropriate amounts of TRGO were added to the LLDPE-*g*-MAn and LLDPE-*g*-Py matrices to obtain compositions ranging from 0.5 to 4.0 wt %. This corresponded to about 0.2 and 1.67 vol %, respectively, calculated using the equation

$$\phi = \frac{d_m W_f}{(d_m - d_f)W_f + d_f} \quad (1)$$

where ϕ is the volume fraction, W_f is the filler's weight fraction, d_m is the density of LLDPE (0.92 g/cm^3), and d_f is the density of the TRGO (assumed to be that of graphite, 2.26 g/cm^3).[28] The melt temperature and torque were continuously recorded during mixing. After preparation, the nanocomposites were placed in a desiccator to prevent moisture absorption prior to further testing.

2.5. Characterization. The ATR-FTIR spectra for the bulk as-prepared particles were obtained on a Varian Scimitar 1000 FTIR equipped with the Pike MIRacle ZnSe ATR accessory. The resolution for each spectrum was 2 cm^{-1} and the number of coadded scans was 24. The spectra presented were baseline corrected and converted to the absorbance mode.

Thermogravimetric analysis was carried out with a Q500 TGA apparatus by TA Instruments. Samples (10 ± 0.5 mg) were heated from ambient temperature to 700 °C under a 50 mL·min^{-1} flow of N_2. A heating rate of 20 °C·min^{-1} was used and continuous recordings of the heat flow, sample temperature, sample weight and its time derivative were taken. All measurements were repeated at least three times.

Raman studies were performed using a HORIBA Jobin Yvon micro-Raman Spectrometer (model: LabRAM) equipped with a 632 nm He/Ne laser source, 1800 1/nm grating and an Olympus BX41 microscope system. The laser power was kept at 0.17 mW. Collection of the spectra was performed in the backscattered mode with the use of a filter at room temperature under the following conditions: ×100 microscope objective, 100 μm pinhole size, 300 μm slit width, and 30 min exposure time. Each spectrum represents the average of two measurements.

Wide-angle X-ray diffraction patterns were measured on a Phillips X'Pert Pro multipurpose diffractometer using Ni-filtered Cu Kα 1,2 radiation (λ_1 = 1.5406 Å, λ_2 = 1.5444 Å) operated at 45 kV and 40 mA with a fixed divergence slit width of 0.5°, 0.02 rad soller slit, 15 mm mask, 2 s revolution, and 40 s count time. Samples were prepared on flat borosilicate glass discs and the diffraction data were collected using a calculated step size of 0.02° from 5° to 90° with an X'pert X'celerator high speed detector. Data were processed using the PanAlytical X'pert HighScore software.

The specific surface area (SSA) of the TRGO particles was determined by Brunauer−Emmett−Teller (BET) characterization. Samples weighing 0.05−0.10 g were first degassed at 110 °C for 24 h and then subjected to a multipoint BET physisorption analysis (Autosorb-1, Quantachrome) for nitrogen relative vapor pressures in the range 0.1−0.3 at 77 K.

TEM imaging of the particles was carried out using a Philips CM 20 electron microscope at an operating voltage of 200 keV. The samples were prepared by depositing a diluted particle dispersion on carbon-coated 300 mesh copper grids and dried at ambient temperature prior to analysis.

Ultrathin films of the composites for TEM characterization were prepared using a Leica ultramicrotome. A FEI Tecnai 20 instrument at an operating voltage of 200 keV was used for TEM imaging. The composite melts were also observed using an Olympus BX 51 optical microscope (Tokyo, Japan). Composite films were loaded on a Linkam SCC 450 hot stage (Surrey, U.K.) at 160 °C and pressed to a thickness of 25 μm. Images were recorded immediately once the desired thickness was reached (5 min), using transmitted light.

Scanning electron microscopy (SEM) of the composites was carried out using a JEOL JMS-840A scanning microscope equipped with an energy-dispersive X-ray (EDX) Oxford ISIS 300 microanalytical system. Samples were gold coated prior to the measurement, with the exception of the already conductive G and TRGO particles. Fractured surfaces of the composites in liquid nitrogen were observed.

Volume resistivity was measured under DC current at room temperature. Samples were prepared by compression molding the melt-compounded composites in a Carver press at 190 °C and 10 MPa to get a thin film of 0.8 mm. Thin composite films with a diameter of 6

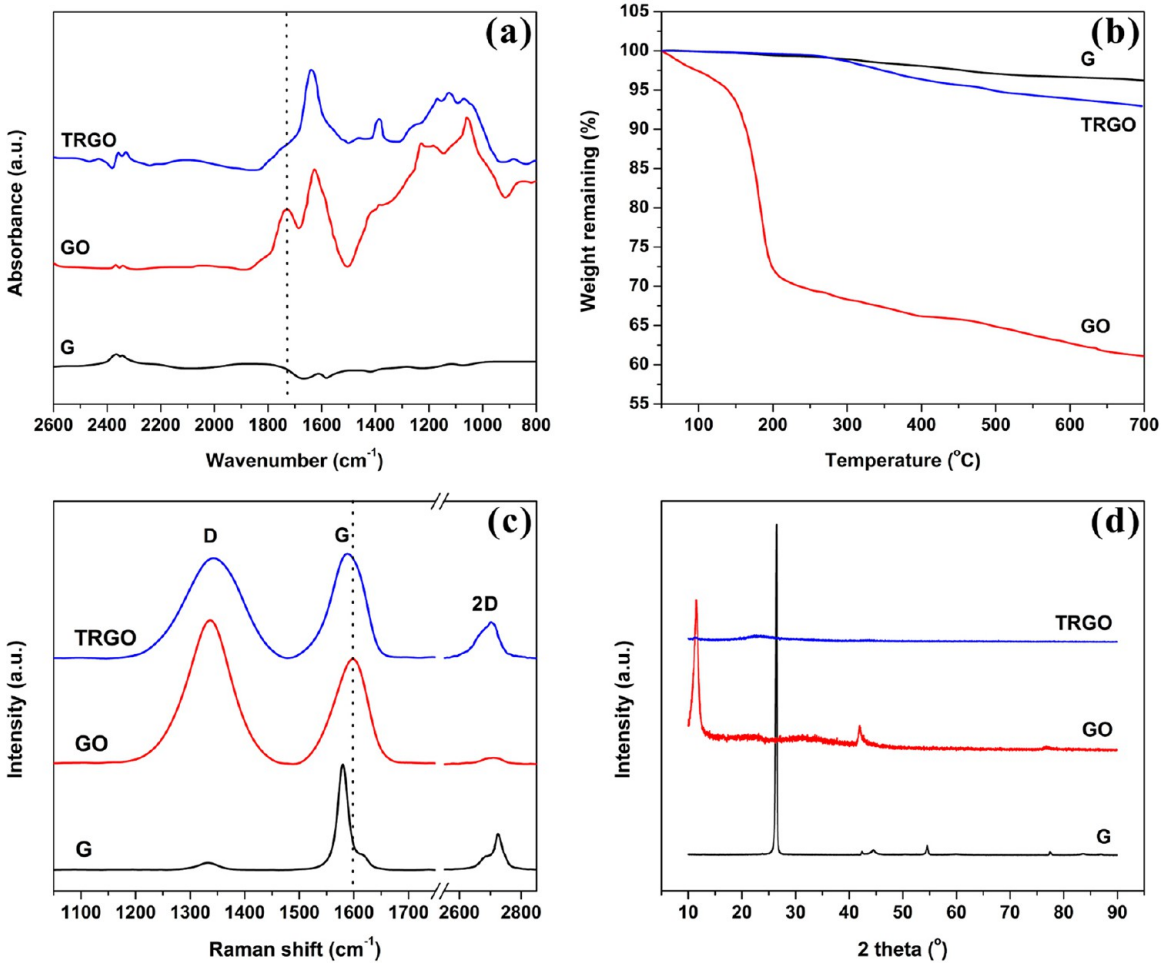

Figure 1. (a) FTIR spectra of G, GO, and TRGO (dotted line: carbonyl stretching vibration absorption band in carboxylic groups, 1729 cm^{-1}). (b) TGA curves of G, GO, and TRGO under nitrogen atmosphere at a heating rate of 20 °C·min^{-1}. (c) Comparison of Raman spectra at 632 nm for bulk G, GO, and TRGO, scaled to have similar height of the G peak. (d) Wide-angle X-ray diffraction patterns of G, GO, and TRGO.

cm were placed inside the measuring chamber (Keithley 8009 Resistivity Test Fixture) of the Keithley 6517B Electrometer/High Resistance Meter (Keithley Instruments, Inc., Cleveland, OH) for an electrification time of 1 min. An Agilent 34401A 6 1/2 Digit multimeter was used for resistivities lower than 10^7 Ω·cm. Sample preparation included cutting test specimens with an area of 1 cm^2 and thickness of 0.04 cm and gold sputtering the surface to reduce contact resistance between the sample and the electrodes of the multimeter. The edges of the samples were trimmed after gold sputtering to prevent short-circuit during the measurement of the resistance (R). The conductivity of the samples was determined from the inverse of resistivity, ρ:

$$\rho = \frac{RA}{l} \tag{2}$$

where A is the contact surface area and l is the average sample thickness.

Rheological characterization was carried out on a Reologica ViscoTech oscillatory rheometer using 20 mm parallel plate fixtures, with a gap of 1 mm at 190 °C. Compression molded disks with a diameter of 20 mm were prepared using the Carver press as described above. Stress sweep experiments were carried out from 1 to 10^3 Pa at a frequency of 0.1 Hz and temperature of 190 °C to identify the limits of linear viscoelasticity. The rheometer was operated in the dynamic oscillatory mode within the linear viscoelasticity region, using stress-controlled experiments. The complex viscosity (η^*), elastic modulus (G'), and tan δ were measured as a function of angular frequency (ω). The reduced storage modulus, G'_r, of the composites, defined as $G'_r = G'/G'_0$, where G'_0 is the storage modulus of the matrix and G' is the modulus of the composite, was calculated at a frequency of 0.1 rad/s.

Tensile properties were measured using an Instron 3369 universal tester, at crosshead speeds of 50 mm·min^{-1}. Dumbbell-shaped specimens were cut with a type-V die according to ASTM D 638 from sheets with average thickness of 3.0 mm, which were prepared by compression molding of the compounded samples at 190 °C and 10 MPa using the Carver press over a period of 5 min.

Thermal analysis of the composites was performed using a differential scanning calorimeter (TA Instruments Q100 Series DSC) calibrated with Indium and Zinc standards. For each measurement, a sample of about 5 ± 0.1 mg was placed in a sealed aluminum pan, and heated to 200 °C at a scanning rate of 20 C·min^{-1}. From these scans, the melting temperature (T_m) and the heat of fusion (ΔH_m) of the nanocomposites were measured. The crystallinity of the samples was calculated using the ΔH_m values with a heat of fusion of 293 J·g^{-1} for fully crystalline polyethylene, after normalization of the nanocomposites' ΔH_m to the actual LLDPE amount. The crystallization temperature (T_c) of the melt was recorded by cooling the samples from 200 to −30 °C at a cooling rate of 10 °C·min^{-1}.

Thermal conductivity values were measured using the apparatus and technique developed by Burheim et al.[38] The thermal conductivity apparatus measures the variables that appear in Fourier's law, that is, the heat flux, the thickness, and the temperature drop over the sample thickness. The heat flux is measured on each side of the sample, together with the temperature drop over the sample and the thickness of the compressed material. Next, the thermal resistance of the sample stack and its contact to the apparatus were calculated from the heat flux and the measured temperature drop. The thermal contact resistance between the samples and the apparatus was separated from the thermal

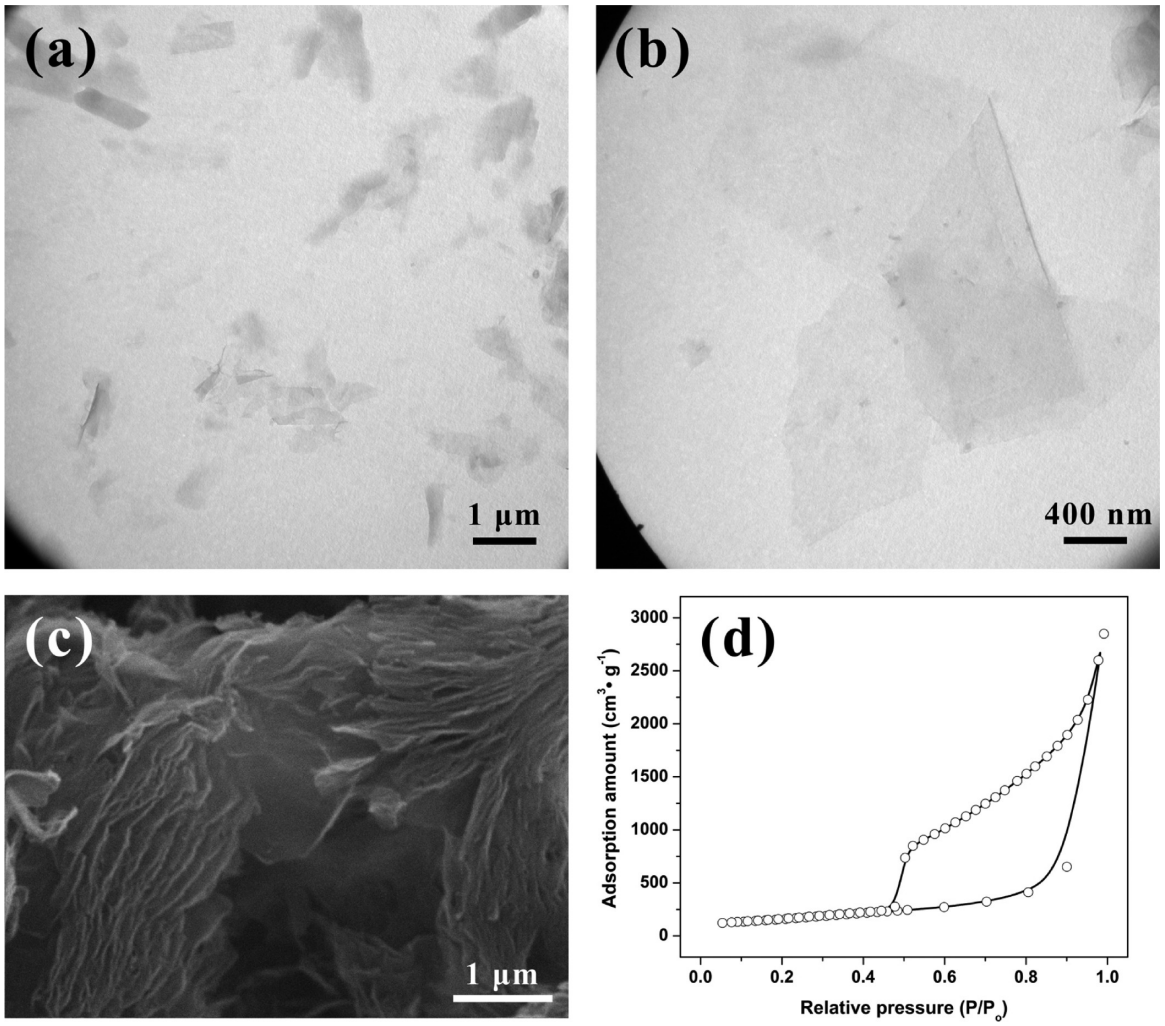

Figure 2. TEM images showing (a) multiple-layered graphene at low magnification and (b) single-layered graphene at high magnification. (c) SEM image showing agglomerated graphene layers. (d) N_2 adsorption−desorption isotherm of the prepared TRGO.

conductivity by plotting the total measured thermal resistance as a function of stack thickness and performing linear regression. The thermal conductivity is equal to the inverse slope of this line. The measurements were carried out at three different compaction pressures, 180, 220, 260, and 300 kPa.

3. RESULTS

3.1. Synthesis and Characterization of TRGO. The oxidation of graphite (G) resulted in the formation of mainly carboxyl and epoxide functional groups on the graphite planes, as well as in the adsorption of water molecules, as shown in the FTIR spectra in Figure 1a.[18] The FTIR spectra of GO showed the presence of O−H stretching vibration of adsorbed water at 1627 cm^{-1}, C═O stretching vibration in carboxyl groups at 1729 cm^{-1}, in-plane deformation vibration of the O−H bond in C−OH groups at 1385 cm^{-1}, C−O−C symmetric stretching of epoxides at about 1228 cm^{-1}, and the C−O stretching vibration in C−OH at 1059 cm^{-1}.[17]

GO was thermally unstable, because of the carboxyl and epoxide functional groups that are bonded to the graphene layers during the oxidation process; an abrupt mass loss of almost 40% attributed to the removal of these groups due to pyrolysis took place within the temperature range of 150−250 °C (Figure 1b). The mass loss of GO up to about 150 °C was almost 5 wt %, attributed to absorbed moisture and residual water in the intergalleries of GO.

These results suggest that most of the oxygen-containing groups are removed at a decomposition temperature between 150 and 250 °C. Lv et al.[35] suggested that the inner stress generated from the removal of the introduced functional groups during the oxidation stage can be further reinforced at temperatures as low as 200 °C by providing a high vacuum environment to obtain the necessary fast exfoliation and stabilization of the individual layers. In the present work, 300 °C was used because it was the lowest temperature at which exfoliation could be achieved (as evident by the abrupt change in volume at this temperature and the final BET surface area values).

Following the vacuum-assisted thermal reduction many of the characteristic peaks of GO disappeared from the FTIR spectra, signifying the removal of most of the functional groups introduced during the oxidation stage. The intensity of the C═O stretching peak at 1729 cm^{-1} was decreased significantly, while the peaks at 1385, 1228, and 1059 cm^{-1} were weakened, probably due to decarboxylation of the carboxyl groups, dehydroxylation of the hydroxyl groups, and thermal decomposition of the epoxy groups at the elevated temperatures of the reduction process. A small amount of adsorbed water was still

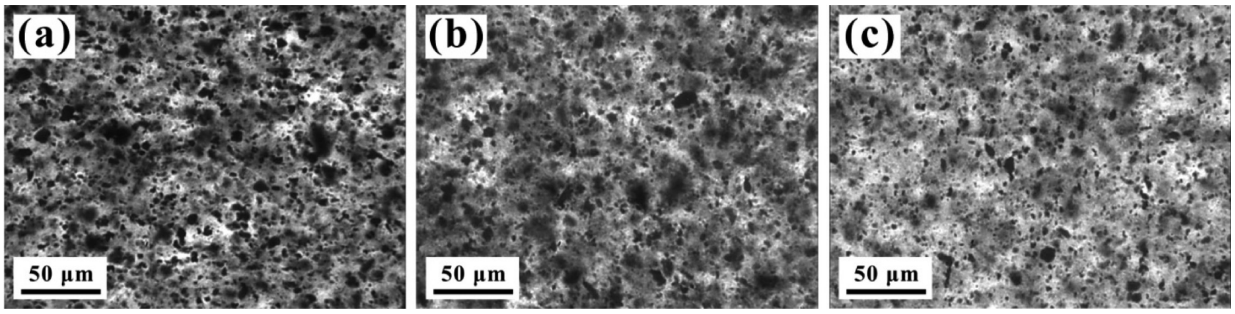

Figure 3. Representative OM images of (a) LLDPE-*g*-MAn(L), (b) LLDPE-*g*-MAn(H), and (c) LLDPE-*g*-Py(L) containing 1.0 wt % TRGO.

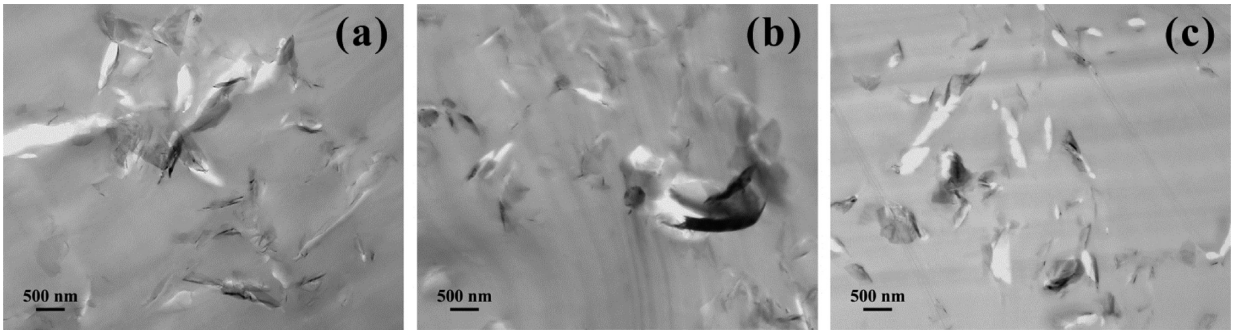

Figure 4. TEM images of composites containing 3 wt % (1.2 vol %) TRGO: (a) LLDPE-*g*-MAn(L) and (b) LLDPE-*g*-MAn(H) showing a mixture of TRGO aggregates and nanoplatelets; (c) LLDPE-*g*-Py(L) containing individually dispersed platelets.

present in TRGO, as evident by the presence of the absorption peak at 1627 cm^{-1}.

As shown in Figure 1b, the TRGO retained 93% of its original weight even after being heated to 700 °C, exhibiting thermal stability similar to pure graphite. These results confirm the reduction of GO during the thermal treatment.

Structural changes during the oxidation and exfoliation process can be followed by Raman spectroscopy. All the Raman spectra (Figure 1c) include the G peak located around 1590 cm^{-1}, caused by the in-plane optical vibration (degenerate zone center E_{2g} mode), and the D peak, located at around 1340 cm^{-1}, associated with the first-order zone boundary phonons.[3,37] Amorphization from graphite to disordered GO led to significant changes of the Raman spectra. The G band became broader and the intensity of the D increased greatly, leading to a much increased D/G intensity ratio, indicative of the presence of defects. Thermal reduction of GO decreased the D/G ratio from 1.36 to 0.94, indicating that the average size of the crystalline graphene (sp^2) domains increased, resulting in partial recovery of the graphitic structure lost during chemical oxidation.[39] Furthermore, the G peak was shifted to lower wavenumbers, from 1598 cm^{-1} for GO to 1588 cm^{-1} for TRGO, substantiating the claim of the sp^2 graphitic structure restoration following reduction.

The resulting TRGO was highly exfoliated, as confirmed by the wide-angle X-ray diffraction (WAXD) patterns presented in Figure 1d. The parent graphite exhibited a sharp and intense peak located at $2\theta = 26.4°$ (002), which was shifted to $2\theta \sim 11.5°$ (002) in GO by the oxidation reaction, revealing an increase of the interlayer spacing from 0.34 to ~0.77 nm, due to incorporation of functional groups and intercalation of water molecules. In contrast, the prepared TRGO did not show any prominent diffraction peak between $2\theta = 10–90°$; the sharp peak at $2\theta \sim 11.5°$ (002) of GO disappeared. This indicates absence of periodic order in TRGO attributed to the extensive thermal exfoliation, which is caused by the rapid degradation of the attached functional groups and facilitated by the applied high vacuum. A very weak and wide reflection centered around $2\theta = 23^o$ signifies the presence of a very small fraction of stacked graphene or "turbostratic" graphite.[19]

TEM images (Figure 2a and b) confirm that GO was exfoliated to a large extent. Few layers of stacked graphene sheets are visible in Figure 2a, whereas single layers are shown in Figure 2b. Lv et al.[35] reported that TRGO obtained by the thermal exfoliation technique consists of a mixture of single-layered and multiple-layered graphene. These graphene layers interact to form micrometer-scale agglomerated structures, as shown in the SEM image (Figure 2c).

The existence of an aggregated structure of graphene layers, which form an open pore system, is also inferred by the type II BET isotherm (Figure 2d), which indicates the absence of micropores or small mesopores, and the existence of asymmetrical slit-shaped pores of large size.[35] Furthermore the 2D Raman band at 2600–2800 cm^{-1} (Figure 1c) is characteristic of the presence of a few layers in the isolated bulk TRGO.

The specific surface area of the TRGO was measured using the N_2 cryo-adsorption/desorption method, yielding a BET value of 586 $m^2 \cdot g^{-1}$. This is comparable to conventionally prepared TRGO (~700 m^2/g)[3−5,10] and indicates a high degree of exfoliation.

3.2. Effect of Polymer Functionalization and Viscosity on Nanocomposite Properties. Investigation of the macroscale dispersion of TRGO in both the high and low viscosity matrices using optical microscopy (OM) (Figure 3) revealed extensive agglomeration, with agglomerates as large as 10−15 μm. This suggests that the graphene aggregates could not be efficiently broken up during melt compounding with the LLDPE matrix, irrespective of viscosity. TRGO aggregates, together with some individually dispersed TRGO platelets are seen in the TEM images (Figure 4a and b). These observations point to a

mechanism of erosion of small fragments or individual platelets from the agglomerates, which takes place together with the rupture or shutter mechanisms that result in breakage of the agglomerates into smaller aggregates.[40]

Introduction of aromatic moieties to the LLDPE resulted in more effective breakup of the filler agglomerates, as seen in Figure 3c. Given that the rheological properties of the maleated and pyridine-functionalized LLDPE remained unaltered,[32] the improvement in dispersion is attributed to the strong interfacial interactions caused by noncovalent $\pi-\pi$ stacking between the aromatic moieties within LLDPE-*g*-Py and the surface of the TRGO. The enhanced interactions resulted in more efficient stress transfer to the TRGO during compounding.

Improved dispersion is also evident at the nanoscale by observing the TEM images of Figure 4c. Based on the TEM images, it is clear that the LLDPE-*g*-MAn/TRGO composites consisted of aggregates and nanoplatelets that were in contact with each other (Figure 4a), whereas a better dispersion and distribution of individual platelets (Figure 4c) is evident in the LLDPE-*g*-Py/TRGO composites. This suggests improved wetting and infiltration[40] of the TRGO agglomerates by the LLDPE-g-Py melt, as a result of the more favorable interactions at the matrix−filler interface, which resulted in lower interfacial tension between polymer and filler.

Furthermore the Raman spectra of the composites containing the pyridine functionalized matrix, LLDPE-*g*-Py, showed a slight shift of the G- band peak to higher wavenumbers (Figure 5). The

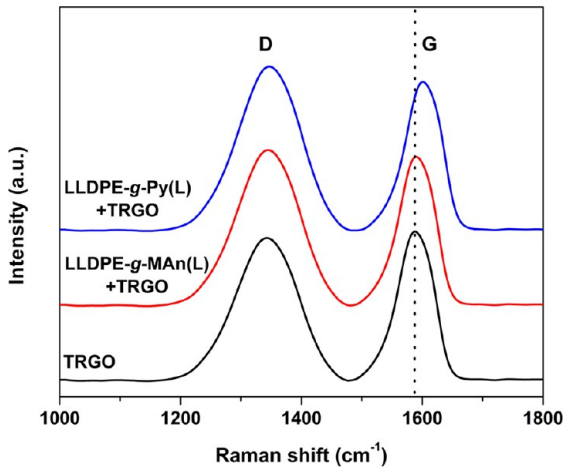

Figure 5. Raman spectra of TRGO, LLDPE-*g*-MAn(L) and LLDPE-*g*-Py(L) composites containing 3.0 wt % TRGO. The dotted line is centered on the G-band peak of TRGO.

shift provides evidence of the $\pi-\pi$ interactions between the aromatic groups of the TRGO and the pyridine. Deformation of the graphene structure by compression forces,[41] resulting from improved infiltration of the polymer melt within the graphene aggregates, may have also contributed to the observed shift.

Addition of TRGO to the polymer resulted in substantial electrical conductivity increases. Maximum values of conductivities of the order of 10^{-4} ($S \cdot m^{-1}$), corresponding to static dissipative materials, were measured irrespective of the type of matrix type (Figure 6). The electrical and rheological percolation curves of the composites are shown in Figures 6 and 7. The percolation thresholds, summarized in Table 1, were estimated from the electrical and rheological percolation curves, shown in Figures 6 and 7 by fitting power-law relations to conductivity data above and below the critical percolation concentration, as described previously.[32] Both electrical and rheological percolation thresholds were below 1 vol % and did not differ significantly from each other. Generally, geometrical percolation in composites containing fillers such as MWCNT takes place at lower concentrations than the electrical percolation, because it does not require direct contact between the filler particles, contrary to electrical percolation which needs direct contact or proximity of the nanotubes, to allow for electron hopping across nanotubes. However in the present case both the electrical and rheological percolation thresholds were very similar. Owing to the high aspect ratio of the graphene platelets interconnectivity is established at very low TRGO contents and therefore both rheological and electrical percolation thresholds coincide.

The very low percolation thresholds are attributed to the microstructure of the composites, which comprises of TRGO aggregates, interconnected with high aspect ratio individually dispersed platelets (Figure 4a and b and schematic, Figure 6). As discussed previously,[32] percolation is promoted in the presence of aggregated structures that are interconnected by individual particles and when a phase-separated, cocontinuous morphology comprising of graphene-rich and poor phases exists.[19]

Functionalization with pyridine resulted in higher geometrical and electrical percolation thresholds compared to the maleated polymer. This is attributed to the improved filler dispersion in these composites, which resulted in an increased number of individually dispersed platelets and a loss of interconnectivity;[11,32] hence the need for a larger amount of TRGO to reach percolation (Table 1).

Introduction of TRGO to the LLDPE matrix resulted in significant increases in the Young's moduli of the composites and in a small reduction in the tensile stress and elongation at the break point, as expected for this class of composite materials (Figure 8). DSC results (not shown here) did not reveal significant differences between the composites and the pure matrices, thus suggesting that the increases in moduli are attributed exclusively to the reinforcing effect of the filler.

Functionalization of the polyethylene matrix with pyridine improved all properties compared to the maleated polyethylene, suggesting enhanced interfacial adhesion between the matrix and filler. Better dispersion in the LLDPE-*g*-Py/TRGO composites, resulted in substantial improvements in the ductility of the material.

Furthermore, the thermal stability of the LLDPE-*g*-MAn(L)/TRGO composites increased by 33 °C upon introduction of 3 wt % TRGO, compared to the neat polymer (Figure 9). A much more significant increase of 88 °C was noted for the LLDPE-*g*-Py(L) based composites at the same particle loading. This is attributed to the improved dispersion, which leads to a higher surface area of impenetrable TRGO nanoplatelets inside the polymer and, thus to a reduction in permeability of the degradation byproducts, slowing down the degradation reactions.

The thermal conductivity of the composites was increased by a factor of 2 with respect to the pure matrix in the LLDPE-*g*-MAn(L)/TRGO, as shown in Figure 10. The increase was more pronounced in the TRGO/LLDPE-*g*-Py composites containing higher amounts of TRGO.

4. DISCUSSION

Following their synthesis by employing thermal exfoliation and reduction, or solution techniques, graphene platelets tend to associate with each other, thus forming aggregates.[35,42] This

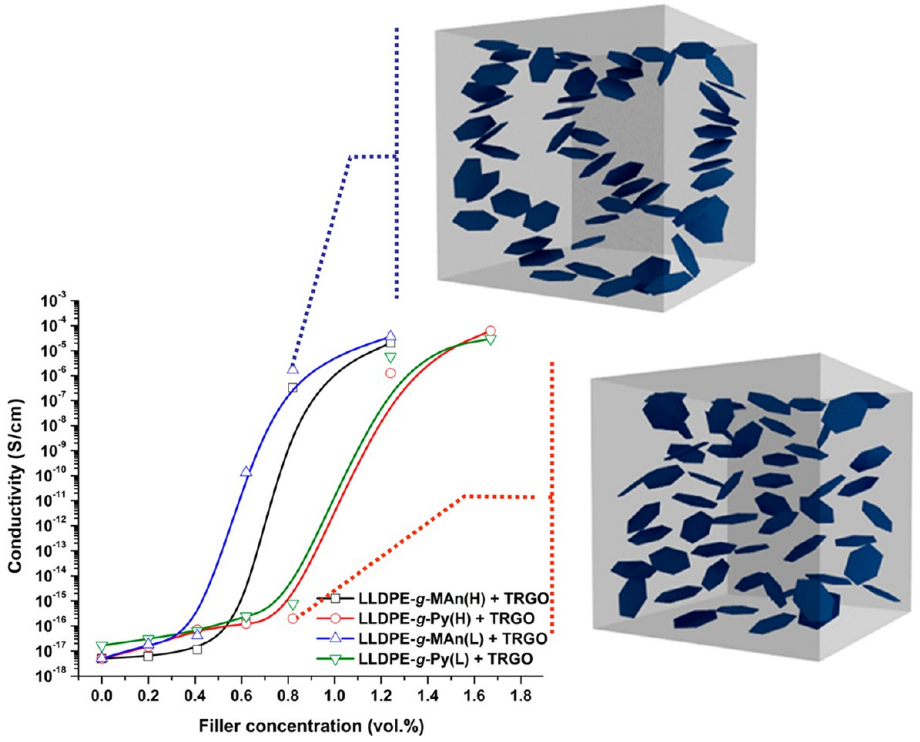

Figure 6. Electrical conductivity as a function of TRGO concentration, showing the effect of microstructure on the electrical percolation threshold of the composites. Solid lines denote fits obtained by fitting power-law equations above and below the percolation threshold.[32]

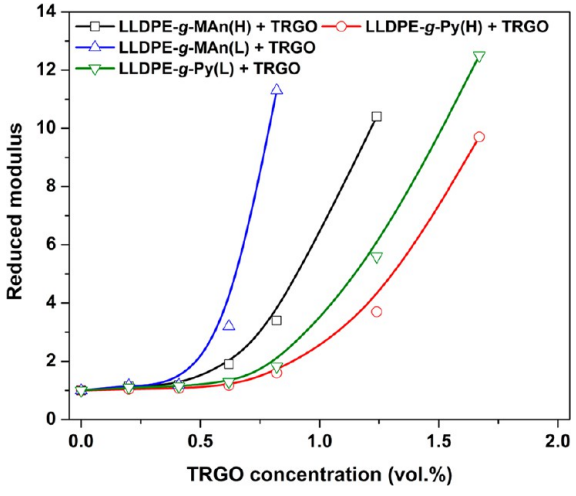

Figure 7. Reduced storage modulus ($G_r' = G'/G_0'$) vs TRGO concentration at 0.1 rad·s^{-1} and 190 °C. Solid lines denote fits obtained by using power-law equations.[32]

Table 1. Electrical and Geometrical Percolation Thresholds, Obtained by Fitting Power-Law Equations[32] below and above the Percolation Threshold

	electrical percolation		geometrical percolation	
sample	ϕ_c (vol %)	w_c (wt %)	ϕ_g (vol %)	w_g (wt %)
LLDPE-*g*-MAn(H)	0.7	1.7	0.6	1.5
LLDPE-*g*-Py(H)	0.9	2.3	0.9	2.2
LLDPE-*g*-MAn(L)	0.5	1.3	0.5	1.2
LLDPE-*g*-Py(L)	0.9	2.2	0.8	1.9

makes their dispersion within the polymer matrix by melt compounding problematic.

A comparison between the LLDPE/TRGO composites presented in this work, and LLDPE/MWCNT composites based on identical matrices and compounding conditions, presented previously,[32] reveals that dispersion of MWCNT by melt compounding was more efficient. Considering that the matrices and compounding procedure were the same, any differences observed must be attributed to the properties of the fillers, which have completely different geometry, specific surface area and aspect ratios.

Generally, the filler dispersion within a polymer matrix involves various steps, including wetting of the initial agglomerates, infiltration of polymer chains within the agglomerated structure, dispersion of the weakened agglomerates, and the distribution of the individual particles into the matrix. These processes have been described in detail by Alig et al.[40] for carbon nanotube agglomerates, but the mechanisms should be similar in the case of TRGO.

Dispersion of the agglomerates depends on their strength of adhesion, which must be counteracted by the external stresses generated by the viscous flow during compounding. Agglomerates will be dispersed if the external stress generated by the viscous flow, $\eta\dot{\gamma}$, is larger than the agglomerate strength, σ_m. The relationship between the two stresses can be characterized by the dimensionless fragmentation number, Fa = $\eta(\dot{\gamma}/\sigma_m)$ which depends on the matrix viscosity, η, the shear rate, $\dot{\gamma}$, and the maximum strength of the agglomerates, σ_m.[40] For Fa $\gg$ 1, rupture or shutter mechanisms, which are characterized by breakage of the large agglomerates into smaller ones, are predominant. Smaller agglomerates continue to undergo rupture until individual particles are obtained. For Fa $\ll$ 1, erosion, where smaller fragments or individual particles separate from the agglomerate surface, is the prevailing mechanism.

Our previous work[32] showed that dispersion of MWCNTs was facilitated significantly by increasing the matrix viscosity.

dx.doi.org/10.1021/am404979g | ACS Appl. Mater. Interfaces 2014, 6, 1916−1925

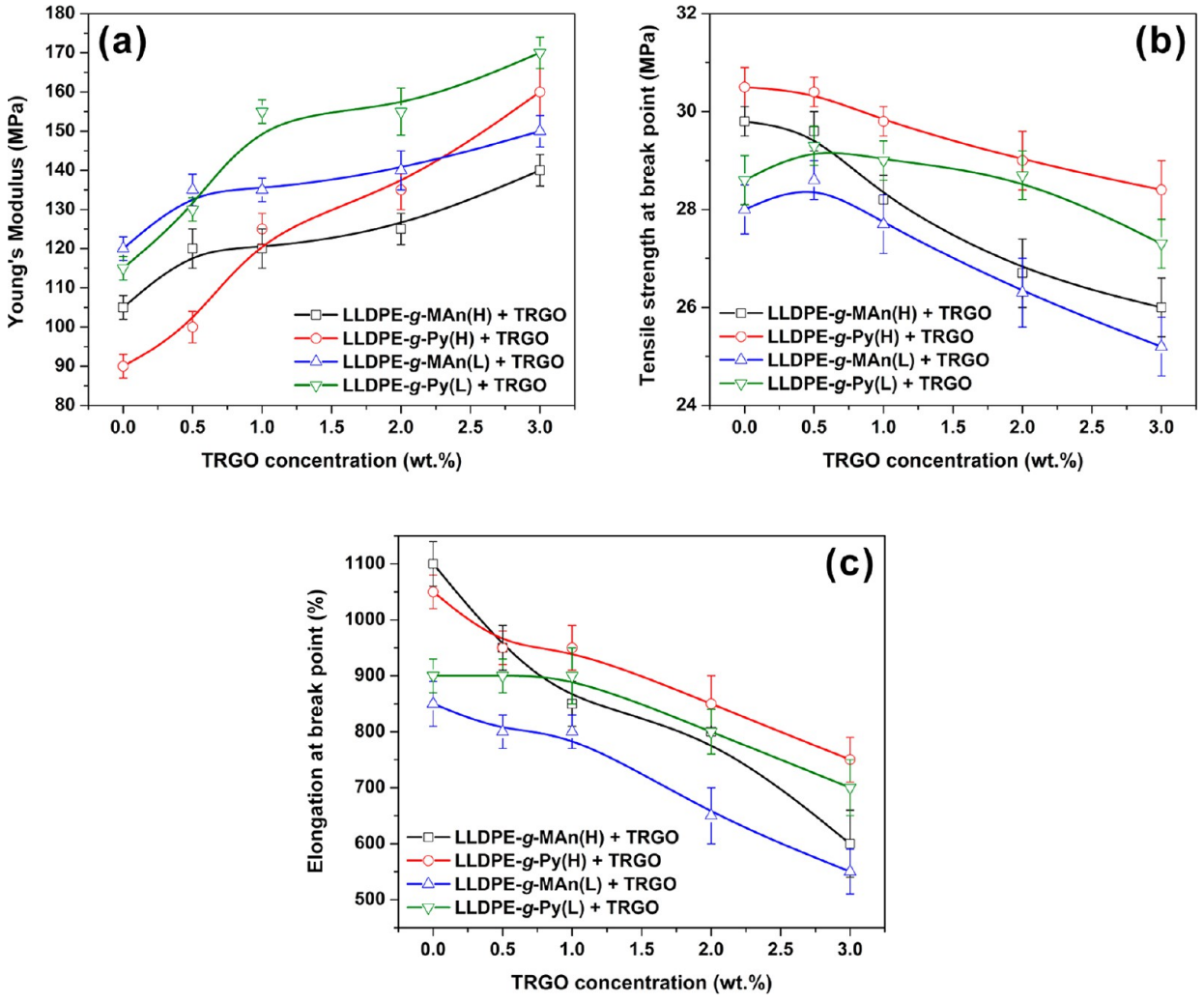

Figure 8. (a) Young's modulus, (b) tensile stress at the break point, and (c) elongation at the break point of the LLDPE/TRGO composites.

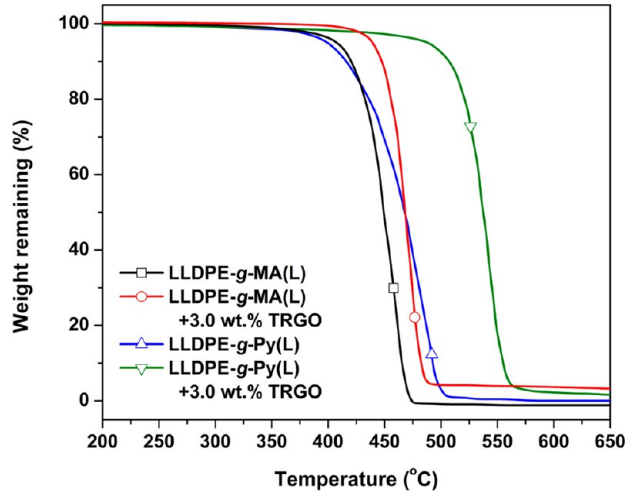

Figure 9. TGA curves of the pure polymers and composites containing 3.0 wt % TRGO under N_2 atmosphere with a heating rate of 20 °C·min^{-1}.

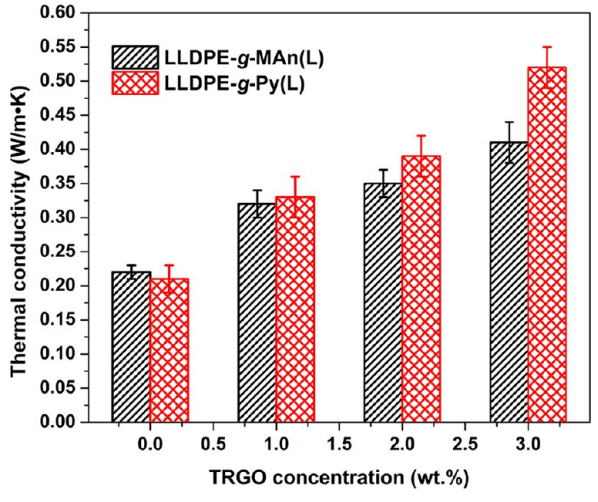

Figure 10. Thermal conductivity as a function of TRGO concentration.

Therefore, the increase in viscosity was sufficient to generate external stresses during compounding that were larger than the agglomerate strength, and values of Fa that were larger than 1. This means that rupture or shutter mechanisms, which resulted in breakage of the MWCNT agglomerates into smaller aggregates and finally individual nanotubes, were predominant.

On the contrary, in the case of graphene aggregates, a mechanism of erosion was predominant, based on the OM and TEM imaging, which showed some individual nanoplatelets, together with the presence of large agglomerates and aggregates.

dx.doi.org/10.1021/am404979g | ACS Appl. Mater. Interfaces 2014, 6, 1916−1925

This implies that the strength of the TRGO agglomerates was much higher, due to the very high surface area of the high aspect ratio platelets, which are strongly associated together, resulting in values of the Fa number that are less than one. Given the predominance of the agglomerate strength, the effect of viscosity would be minimal in this case and larger shear rates would be needed during compounding to achieve agglomerate breakup. This was indeed confirmed in this work in the TRGO composites based on high and low viscosity LLDPE matrices.

In both MWCNT and TRGO composites, there was a favorable effect of noncovalent interactions when the LLDPE matrix was functionalized with pyridine. Wetting and infiltration of the initial agglomerates by the polymer melt depends on the interfacial energy.[40] Functionalization lowered the interfacial tension, thus enhancing both the initial wetting of the agglomerates and their infiltration. This weakened the interparticle interactions and, thus, less energy was required to break-up the agglomerates.

The comparison between the electrical percolation thresholds of MWCNT and TRGO composites with LLDPE shown in Figure 11 revealed that, as expected, the 2-D graphene

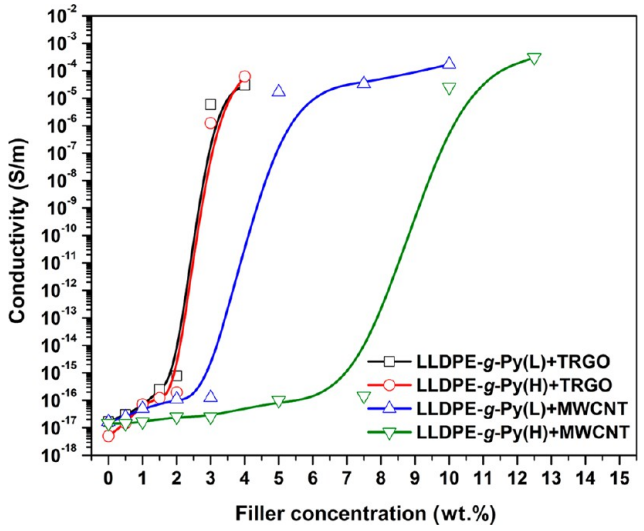

Figure 11. Comparison of electrical conductivity as a function of filler concentration for LLDPE/TRGO and LLDPE/MWCNT composites.

nanosheets had lower percolation thresholds than the 1-D carbon nanotubes, irrespective of the viscosity and compatibilization procedure. This is attributed to the high aspect ratio of the TRGO.[25]

Based on these results, TRGO appears advantageous in terms of percolation threshold, whereas its maximum conductivity is slightly lower by about an order of magnitude, compared to the equivalent MWCNT-based composites. The presence of residual oxygen in TRGO may be responsible for the lower conductivity.

In terms of mechanical properties, TRGO-based composites had higher moduli compared to their MWCNT counterparts (Figure 12) at the same filler loadings, due to the higher surface area and aspect ratio of TRGO, while the elongations at break were comparable. The mechanical properties of LLDPE/TRGO composites, combined with their lower electrical percolation threshold, make them more advantageous than their counterparts containing multiwalled carbon nanotubes (MWCNT), because lower amounts of TRGO are needed to achieve electrical

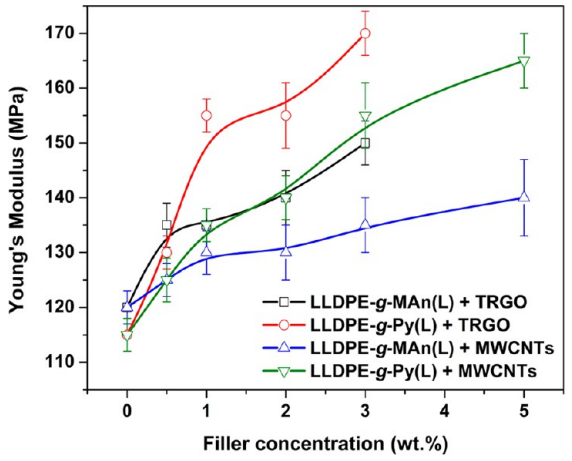

Figure 12. Comparison of Young's modulus as a function of filler concentration between LLDPE/TRGO and LLDPE/MWCNT composites.

conductivity and improved modulus, without compromising their ductility.

These features are desired when a combination of good engineering properties together with electrical conductivity are needed, for example, in structural applications or in automotive or aerospace components. Even though in the present work the matrices used consisted entirely of functionalized polyethylene, a melt compounding approach using small amounts of the pyridine-functionalized polyolefin as a compatibilizer may also be a promising alternative to further lower the cost of the composites.

5. CONCLUSIONS

Thermally reduced graphene was produced at 300 °C under high vacuum. The resulting product had a specific surface area of 586 m^2/g and was highly exfoliated, as evident by XRD and TEM characterization.

TRGO was incorporated into two maleated LLDPE matrices, having high and low viscosity and to their respective amino-pyridine derivatives by melt compounding. Large aggregates formed when the maleated matrices were used, irrespective of their viscosity, indicative of the tendency of the graphene nanoplatelets to associate with each other. The noncovalent compatibilization procedure, involving interactions between the aromatic moieties on the pyridine grafted matrix through $\pi-\pi$ stacking with the surface of TRGO, resulted in a reduction in the size of the aggregates. Imaging revealed individual nanoplatelets in the melt, suggesting that the TRGO aggregates break up through an erosion mechanism.

The LLDPE/TRGO composites exhibited very low electrical percolation thresholds, between 0.5 and 0.9 vol %, depending on the matrix viscosity and the presence of functional groups. Better dispersion in the compatibilized composites resulted in a slight increase in the rheological and electrical percolation thresholds and to a significant improvement in mechanical properties, including modulus and elongation at break, with respect to their noncompatibilized counterparts. A significant enhancement in the thermal stability of the composites was also noted in the compatibilized composites, while the rest of the thermal properties were not affected. Finally, addition of TRGO resulted in increases in the thermal conductivity of the composites, with the compatibilized composites showing a more substantial effect.

dx.doi.org/10.1021/am404979g | ACS Appl. Mater. Interfaces 2014, 6, 1916−1925

AUTHOR INFORMATION

Corresponding Author

*Tel.: 613-533-3079. Fax: 613-533-3079. E-mail: kontopm@queensu.ca.

Notes

The authors declare no competing financial interest.

ACKNOWLEDGMENTS

Financial support from the Natural Sciences and Engineering Research Council of Canada (NSERC) through the Discovery and Accelerator Supplement programs is gratefully acknowledged. The polymers used in this study were donated by E.I. DuPont Canada.

REFERENCES

(1) Spitalsky, Z.; Tasis, D.; Papagelis, K.; Galiotis, C. *Prog. Polym. Sci.* **2010**, *35*, 357−401.
(2) Sahoo, N. G.; Rana, S.; Cho, J. W.; Li, L.; Chan, S. H. *Prog. Polym. Sci.* **2010**, *35*, 837−867.
(3) Zhu, Y.; Murali, S.; Cai, W.; Li, X.; Suk, J. W.; Potts, J. R.; Ruoff, R. S. *Adv. Mater.* **2010**, *22*, 3906−3924.
(4) Singh, V.; Joung, D.; Zhai, L.; Das, S.; Khondaker, S. I.; Seal, S. *Prog. Mater. Sci.* **2011**, *56*, 1178−1271.
(5) Edwards, R. S.; Coleman, K. S. *Nanoscale* **2013**, *5*, 38−51.
(6) Zhang, W.; Wang, C.; Li, Z.; Lu, Z.; Li, Y.; Yin, J.-J.; Zhou, Y.-T.; Gao, X.; Fang, Y.; Nie, G.; Zhao, Y. *Adv. Mater.* **2012**, *24*, 5391−5397.
(7) Kim, H.; Abdala, A. A.; Macosko, C. W. *Macromolecules* **2010**, *43*, 6515−6530.
(8) Huang, X.; Qi, X.; Boey, F.; Zhang, H. *Chem. Soc. Rev.* **2012**, *41*, 666−686.
(9) Potts, J. R.; Dreyer, D. R.; Bielawski, C. W.; Ruoff, R. S. *Polymer* **2011**, *52*, 5−25.
(10) Huang, X.; Yin, Z.; Wu, S.; Qi, X.; He, Q.; Zhang, Q.; Yan, Q.; Boey, F.; Zhang, H. *Small* **2011**, *7*, 1876−1902.
(11) Potts, J. R.; Shankar, O.; Du, L.; Ruoff, R. S. *Macromolecules* **2012**, *45*, 6045−6055.
(12) Ha, H. W.; Choudhury, A.; Kamal, T.; Kim, D.-H.; Park, S.-Y. *ACS Appl. Mater. Interfaces* **2012**, *4*, 4623−4630.
(13) Kim, H.; Macosko, C. W. *Polymer* **2009**, *50*, 3797−3809.
(14) Yan, D.; Zhang, H.-B.; Jia, Y.; Hu, J.; Qi, X.-Y.; Zhang, Z.; Yu, Z.-Z. *ACS Appl. Mater. Interfaces* **2012**, *4*, 4740−4745.
(15) Wan, C.; Chen, B. *J. Mater. Chem.* **2012**, *22*, 3637−3646.
(16) Song, W.-L.; Veca, L. M.; Kong, C. Y.; Ghose, S.; Connell, J. W.; Wang, P.; Cao, L.; Lin, Y.; Meziani, M. J.; Qian, H.; LeCroy, G. E.; Sun, Y.-P. *Polymer* **2012**, *53*, 3910−3916.
(17) Appel, A.-K.; Thomann, R.; Müelhaupt, R. *Polymer* **2012**, *53*, 4931−4939.
(18) El Achaby, M.; Arrakhiz, F.-E.; Vaudreuil, S.; el Kacem Qaiss, A.; Bousmina, M.; Fassi-Fehri, O. *Polym. Compos.* **2012**, *33*, 733−744.
(19) Kim, H.; Kobayashi, S.; AbdurRahim, M. A.; Zhang, M. J.; Khusainova, A.; Hillmyer, M. A.; Abdala, A. A.; Macosko, C. W. *Polymer* **2011**, *52*, 1837−1846.
(20) Huang, Y.; Qin, Y.; Wang, N.; Zhou, Y.; Niu, H.; Dong, J.-Y.; Hu, J.; Wang, Y. *Macromol. Chem. Phys.* **2012**, *213*, 720−728.
(21) Shevchenko, V. G.; Polschikov, S. V; Nedorezova, P. M.; Klyamkina, A. N.; Shchegolikhin, A. N.; Aladyshev, A. M.; Muradyan, V. E. *Polymer* **2012**, *53*, 5330−5335.
(22) Kuila, T.; Bose, S.; Hong, C. E.; Uddin, M. E.; Khanra, P.; Kim, N. H.; Lee, J. H. *Carbon* **2011**, *49*, 1033−1037.
(23) Kuila, T.; Bose, S.; Mishra, A. K.; Khanra, P.; Kim, N. H.; Lee, J. H. *Polym. Test.* **2012**, *31*, 31−38.
(24) Stüerzel, M.; Kempe, F.; Thomann, Y.; Mark, S.; Enders, M.; Müelhaupt, R. *Macromolecules* **2012**, *45*, 6878−6887.
(25) Steurer, P.; Wissert, R.; Thomann, R.; Müelhaupt, R. *Macromol. Rapid Commun.* **2009**, *30*, 316−327.
(26) El Achaby, M.; Qaiss, A. *Mater. Des.* **2013**, *44*, 81−89.
(27) Cheng, S.; Chen, X.; Hsuan, Y. G.; Li, C. Y. *Macromolecules* **2012**, *45*, 993−1000.
(28) Ma, J.; Meng, Q.; Michelmore, A.; Kawashima, N.; Izzuddin, Z.; Bengtsson, C.; Kuan, H.-C. *J. Mater. Chem. A* **2013**, *1*, 4255−4264.
(29) Tasis, D.; Tagmatarchis, N.; Bianco, A.; Prato, M. *Chem. Rev.* **2006**, *106*, 1105−1136.
(30) Su, Q.; Pang, S.; Alijani, V.; Li, C.; Feng, X.; Muellen, K. *Adv. Mater.* **2009**, *21*, 3191−3195.
(31) Osazuwa, O.; Petrie, K.; Kontopoulou, M.; Xiang, P.; Ye, Z.; Docoslis, A. *Compos. Sci. Technol.* **2012**, *73*, 27−33.
(32) Vasileiou, A. A.; Docoslis, A.; Kontopoulou, M.; Xiang, P.; Ye, Z. *Polymer* **2013**, *54*, 5230−5240.
(33) Zhang, C.; Lv, W.; Xie, X.; Tang, D.; Liu, C.; Yang, Q.-H. *Carbon* **2013**, *62*, 11−24.
(34) Zhang, H.-B.; Wang, J.-W.; Yan, Q.; Zheng, W.-G.; Chen, C.; Yu, Z.-Z. *J. Mater. Chem.* **2011**, *21*, 5392−5397.
(35) Lv, W.; Tang, D.-M.; He, Y.-B.; You, C.-H.; Shi, Z.-Q.; Chen, X.-C.; Chen, C.-M.; Hou, P.-X.; Liu, C.; Yang, Q.-H. *ACS Nano* **2009**, *3*, 3730−3736.
(36) Wong, C. H. A.; Ambrosi, A.; Pumera, M. *Nanoscale* **2012**, *4*, 4972−4977.
(37) Banhart, F.; Kotakoski, J.; Krasheninnikov, A. V *ACS Nano* **2011**, *5*, 26−41.
(38) Burheim, O. S.; Ellila, G.; Fairweather, J. D.; Labouriau, A.; Kjelstrup, S.; Pharoah, J. G. *J. Power Sources* **2013**, *221*, 356−365.
(39) Ganguly, A.; Sharma, S.; Papakonstantinou, P.; Hamilton, J. *J. Phys. Chem. C* **2011**, *115*, 17009−17019.
(40) Alig, I.; Pötschke, P.; Lellinger, D.; Skipa, T.; Pegel, S.; Kasaliwal, G. R.; Villmow, T. *Polymer* **2012**, *53*, 4−28.
(41) Cohen, E.; Ophir, A.; Kenig, S.; Barry, C.; Mead, J. *Macromol. Mater. Eng.* **2013**, *298*, 419−428.
(42) Khan, U.; Porwal, H.; O'Neill, A.; Nawaz, K.; May, P.; Coleman, J. N. *Langmuir* **2011**, *27*, 9077−9082.